# Approaching Optimal Light Evolution at Adiabaticity Control Limit in Inverse-Designed Waveguides

Xuanyu Liu, Wange Song,[*] Jiacheng Sun, Shengjie Wu, Yichen Zhu, Zhiyuan Lin,
Chunyu Huang, Shining Zhu, and Tao Li[†]
*National Laboratory of Solid State Microstructures, Key Laboratory of Intelligent Optical Sensing*
*and Manipulations, Jiangsu Key Laboratory of Artificial Functional Materials, College of Engineering*
*and Applied Sciences, Collaborative innovation center of advanced microstructures,*
*Nanjing University, Nanjing, 210093, China*

(Received 26 June 2025; revised 2 October 2025; accepted 1 December 2025; published 22 December 2025)

Controlling state evolution via adiabaticity has attracted significant interest for its vital role in quantum and photonic applications. However, attaining the *adiabaticity control limit* (ACL)—defined as the shortest possible duration with minimal mode crosstalk during evolution—remains a significant challenge. In this Letter, we address this issue by introducing an inverse adiabaticity control strategy, where the tolerable crosstalk serves as a control parameter. Taking the stimulated raman adiabatic passage as an example, we demonstrate the principle of inverse adiabaticity control and determine the map of optimal solution under various parameter constraints. The effectiveness and superiority of the inverse design strategy are experimentally demonstrated in silicon photonic waveguides. Crucially, we show that ACL solutions can achieve both the fastest and most robust evolution simultaneously, overcoming the usual tradeoff in conventional forward-designed structures and meeting key needs for photonic and quantum computing devices. The inverse control method offers a universal strategy that may be applicable across a wide range of physical settings.

DOI: 10.1103/zwt9-79zy

Exploring the dynamical evolution of physical states represents a central challenge in fundamental physics [1–11], in which accelerating (non-) adiabatic state evolution toward a prespecified final target has attracted considerable attention in both fundamental physics and practical applications, such as in fast quantum computation in fast quantum computation [12–14] and integrated photonic devices [15–17], etc. Existing strategies include optimizing the evolution path in parameter space under adiabatic conditions [18], or minimizing the total evolution duration to achieve the fastest state transfer [19]. In addition, the framework of shortcuts to adiabaticity (STA) [20,21] has been developed, which deliberately allows partial nonadiabatic transitions for appropriate acceleration, while ultimately enabling high-fidelity access to the target state. Representative STA protocols include the counterdiabatic (CD) method [22–24] and invariant-based inverse engineering (IIE) [25,26], etc.

It is anticipated that efforts to accelerate state evolution will encounter a fundamental optimum. Usually, the state evolution process is governed by two parameters: total evolution time and mode crosstalk. While the optimal scenario is to minimize both, they inherently trade off against each other. For example, adiabatic protocols suppress crosstalk at the cost of long durations, whereas STA shorten the evolution but typically increase crosstalk and parameter sensitivity. It is therefore essential to identify the fundamental bound—the adiabaticity control limit (ACL)—defined as the shortest attainable evolution with minimal crosstalk. Establishing the ACL would deepen the understanding of adiabatic control and guides the design of high-performance photonic and quantum devices.

However, existing conventional designs typically struggle to reach the ACL, resulting in unavoidable redundancy during their state evolution process. This is because these approaches face difficulties in quantitatively controlling the dimension of crosstalk, which prevents them from obtaining a complete map of (non-)adiabatic state evolution. By contrast, inverse design approaches [27–34] offer the potential to control crosstalk—and thus adiabaticity—allowing for the precise determination of the ACL.

In this Letter, we propose an inverse adiabaticity control framework, which introduces a new dimension to control the eigenmode crosstalk and enables identification of the ACL. Using stimulated raman adiabatic passage (STIRAP) as an example, we elaborate on the inverse adiabaticity control strategy and construct a comprehensive map of (non-)adiabatic state evolution, illustrating the landscape of optimal fidelity. Consequently, we reveal for the first time the existence of the ACL, at which the evolution process

---

[*] Contact author: songwange@nju.edu.cn
[†] Contact author: taoli@nju.edu.cn

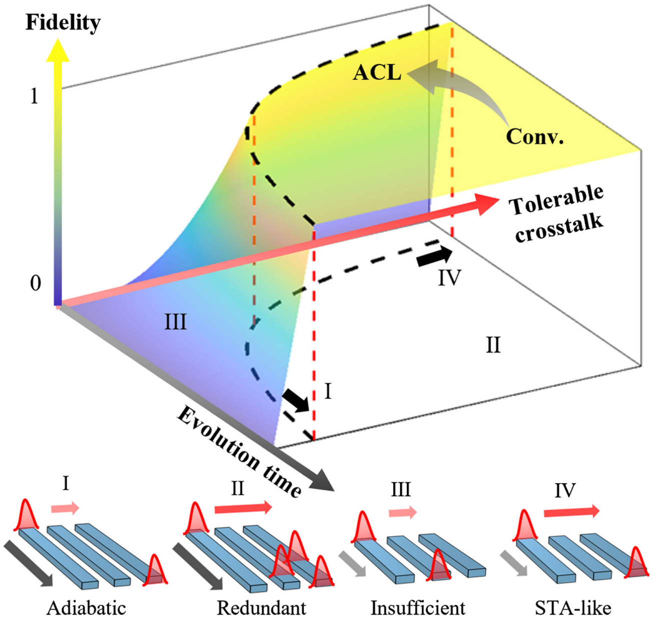

FIG. 1. Schematic illustration of the inverse adiabaticity control. For each pair of evolution time and tolerable crosstalk, there exists an optimal evolution strategy that maximizes fidelity. The lower panel illustrates the four marked typical evolution strategies. The parameter combinations that precisely enable the evolution process to achieve the target form the ACL, which is challenging for conventional designs to reach.

achieves both maximum speed and robustness. We further validate our method experimentally in integrated silicon waveguides, showing clear advantages over conventional design strategies. Importantly, we find that, contrary to conventional understanding, the reduced robustness of conventional STA designs does not stem from degraded adiabaticity. Instead, it arises from redundancy in both duration and crosstalk, as evidenced by the result that the best robustness is achieved on the ACL. Furthermore, our results demonstrate that achieving the most compact and robust state evolution is in fact a unified goal, which is crucial for device design in optical waveguides and other physical platforms.

The basic principle of inverse adiabaticity control is illustrated in Fig. 1. Regardless of specific implementation, a state evolution process has a predetermined target state. Fidelity, defined as the overlap between final output and target state, quantifies the accuracy of the result. A fidelity close to unity is obtained when the output matches the target, while a value near zero indicates complete divergence. In a state evolution process, evolution time and mode crosstalk usually are two key parameters that influence the system's dynamics. The evolution time reflects the longitudinal scale of the system. A longer evolution time provides more opportunity for the modes to evolve. On the other hand, transverse modulation of the system gives rise to mode crosstalk. While crosstalk typically varies during evolution, we can define an *average crosstalk* [35] to quantify its overall degree. By permitting a high level of average crosstalk, the evolution time can be shortened, as seen in the STA process [20]. However, such approaches lack control over the degree of crosstalk, often resulting in excessive crosstalk and reduced robustness. In contrast, inverse design allows us to specify a *tolerable crosstalk*—an upper limit on average crosstalk—which enables quantitative regulation of the system's adiabaticity. This, in turn, enables the optimization of maximum fidelity across all combinations of these parameters (evolution time and tolerable crosstalk), represented by the colored surface in Fig. 1. In fact, Fig. 1 indicates the highest fidelity attainable for a given evolution time and crosstalk bound, and it reveals four representative evolution scenarios, illustrated using waveguide light propagation: (I) Adiabatic evolution that has long duration and low crosstalk, characterized by slow coupling of light in waveguides; (II) redundant evolution, where excessively large values of both parameters cause optical modes to retrace their paths and thus induce unnecessary oscillations; (III) insufficient evolution, in which small parameter values prevent complete transfer of light to the target waveguide output; and (IV) STA-like evolution, where increased tolerable crosstalk between waveguide modes compensates for a shorter evolution time. When both parameters are increased to the point where the fidelity approaches sufficiently close to unity (here taken as 0.99), the existence of the ACL is identified, delineating conditions under which the system achieves the target without redundancy, as exemplified by cases I and IV. Conventional forward-design methods usually fail to reach the ACL and thus fall into case II. To reach the ACL, optimization-based inverse design is indispensable for the ideal high-fidelity outcomes.

In the following, we illustrate our approach using stimulated raman adiabatic passage (STIRAP) as an example. STIRAP, characterized by adiabatic population transfer via dark states, is renowned for enabling noise-resistant quantum operations, making it crucial for quantum control protocols [4,6,7]. This process serves as a suitable model to demonstrate our design, which can be implemented in photonic systems using single-mode waveguide arrays. Specifically, when the optical field overlap between adjacent waveguides is sufficiently small, light propagation in the waveguide array can be described using coupled mode theory (CMT) [36], whose mathematical form closely resembles that of the Schrödinger equation $-i(d/dt)|\psi\rangle = H|\psi\rangle$ with the time variable $t$ replaced by the propagation distance $z$. In the tight-binding CMT equation, $|\psi\rangle = (\psi_1, \psi_2, \psi_3)^T$ denotes the modal amplitudes in each waveguide and $H$ is the system Hamiltonian featuring the propagation constants in each waveguide (diagonal) and the couplings between them (off-diagonal). The total waveguide length $L$ is related to the normalized evolution time as $L = T/c_{\max}$, where $c_{\max}$ is the maximum coupling coefficient in the system.

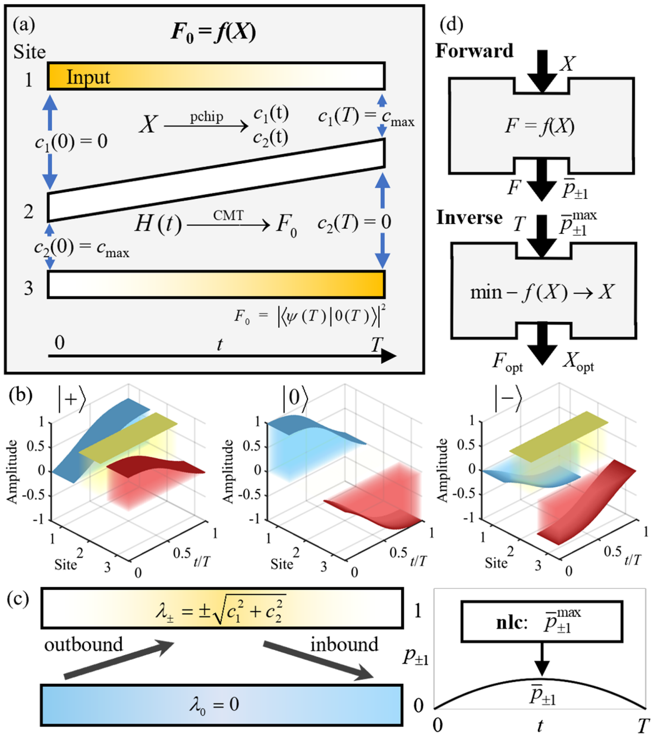

FIG. 2. Inverse design in STIRAP. (a) Optical-waveguide realization of the STIRAP framework. The input $X$ modulates the system Hamiltonian to generate the output fidelity $F_0$. The gradient of colors shows energy transfer from site 1 to site 3. (b) Mode distributions under linear coupling functions $c_1(t) = t/T$ and $c_2(t) = 1\text{-}t/T$. Here $c_1/c_2 = 0 \sim \infty$ for $t = 0 \sim T$. (c) Left: the evolution of eigenstate populations indicated by a color gradient. Right: average crosstalk constrained by a nonlinear condition. (d) Comparisons of design principles. Top: forward design, where input $X$ yields direct outputs ($F$, $\bar{p}_{\pm1}$). Bottom: inverse design, where $T$ and $\bar{p}_{\pm1}^{\max}$ are specified, producing optimal outputs $(F_{\text{opt}}, X_{\text{opt}})$.

In Fig. 2(a), the target of STIRAP is to transfer the dark state input from site 1 to the output at site 3. The coupling coefficients $c_1$ and $c_2$ are modulated by interpolation points $X$, where $c_1$ varies from 0 at the input to the maximum value $c_{\max}$ at the output, while $c_2$ behaves inversely. The fidelity $F_0 = |\langle\psi(T)|0(T)\rangle|^2$, which quantifies the overlap between the output state and the target dark state, is calculated using CMT. As shown in Fig. 2(b), if the system evolves completely adiabatically, the input mode will follow the dark state $|0\rangle = (\cos\theta, 0, -\sin\theta)^T$ throughout the evolution, where $\theta = \arctan(c_1/c_2)$ is the mixing angle. However, any evolution inevitably induces transitions of the dark state to the other two modes $|\pm\rangle = [1/\sqrt{2}](\sin\theta, \pm1, \cos\theta)^T$. To achieve a high-fidelity output, there must be a process where the target state first transitions out to these modes and then converges back to zero-energy level [Fig. 2(c)]. The sum of average population of the other two modes can be defined as the average crosstalk $\bar{p}_{\pm1} = 1 - \bar{p}_0 = 1 - (1/T)\int_0^T |\langle\psi(t)|0(t)\rangle|^2 dt$, where a larger value indicates stronger departure from adiabaticity throughout the entire evolution process. The optimization problem can thus be formulated as

$$\min_{0 \le X_i \le 1} -f(x),$$
$$\text{s.t.}\,\bar{p}_{\pm1}(X) \le \bar{p}_{\pm1}^{\max},\ i = 1, 2, \ldots, N_X, \tag{1}$$

where $f(X)$ is the fidelity function, and $X$ denotes the interpolation points that specify the time-dependent coupling-coefficient profiles $c_1$ and $c_2$ [37]. Both $f(X)$ and $\bar{p}_{\pm1}(X)$ depend explicitly on $X$. The nonlinear inequality constraint in Eq. (1) serves to constrain $\bar{p}_{\pm1}$ to be below the tolerable crosstalk $\bar{p}_{\pm1}^{\max}$ [Fig. 2(c)]. The gradient descent method is used to maximize the fidelity by minimizing $-f(X)$. More detailed optimization settings are provided in Ref. [37].

A key advantage of inverse design is its ability to incorporate such nonlinear constraints. As shown in Fig. 2(d), forward design involves a one-way mapping from an input $X$ to output performance $F$, where $\bar{p}_{\pm1}$ is merely a by-an product. In contrast, both $\bar{p}_{\pm1}^{\max}$ and $T$ are treated as key requirements in inverse design, effectively breaking the unidirectional causal relationship and thereby yielding a richer diversity of optimal solutions $(F_{\text{opt}}, X_{\text{opt}})$. In conventional STA techniques, one passively sustains resultant crosstalk, which has long been regarded as an unintended incidental effect. By contrast, our approach enables advance assessment of whether the crosstalk results meet the constraints. Thus, tolerable crosstalk actually becomes a control parameter in inverse design, enabling systematic exploration of the full fidelity landscape and precise identification of the ACL.

Figure 3(a) shows the inverse-designed results, where the optimal fidelity $F_0$ is obtained over the parameter space, forming in a complete distribution $F_0(\bar{p}_{\pm1}^{\max}, T)$. As both $T$ and $\bar{p}_{\pm1}^{\max}$ increase, the optimal fidelity increases and ultimately approaches unity, delineating the ACL (defined by the $F_0 = 0.99$ contour). This result aligns with the aforementioned schematic in Fig. 1, where the four representative strategies are marked. The evolution of zero-mode population $p_0$ as function of normalized time $t/T$ for these strategies is illustrated in Fig. 3(b) (see Ref. [37] for more details about $p_0$ and coupling coefficient profiles). In case I, the zero-mode population remains consistently high ($p_0 > 0.94$), reaching the target while preserving adiabaticity. In case IV, controlled nonadiabaticity accelerates the evolution, achieving the target in shorter time. In case III, the adiabatic path is preserved but the duration is too short to reach the output. In case II, the target is reached but unnecessary nonadiabatic process is introduced. Through inverse design, the full fidelity landscape is uncovered. The ACL, which represents the most efficient scheme—that is,

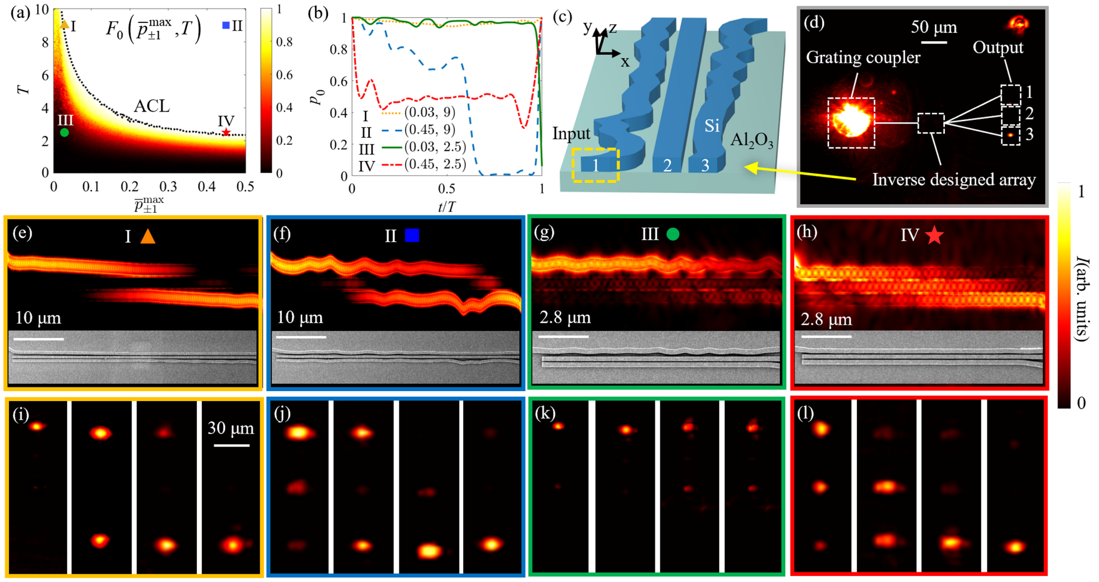

FIG. 3. (a) The optimized fidelity $F_0$ as a function of evolving time $T$ and tolerable crosstalk $\bar{p}_{\pm1}^{\max}$. The dotted line represents the contour of $F_0 = 0.99$, indicating the ACL under this fidelity threshold. Four representative cases (I–IV) are selected for subsequent analysis. (b) The zero-mode population $p_0$ as a function of normalized time $t/T$ under the four cases. (c) Schematics of the inverse designed STIRAP processes on SOI waveguide platform. (d) CCD recorded optical propagation in the waveguide arrays. (e)–(h) Simulated light propagation in the optimized waveguide arrays with corresponding scanning electron microscope (SEM) images for the four cases. (i)–(l) Output intensity at $z = 0.25L$, $0.5L$, $0.75L$, and $L$ corresponding to structures in (e)–(h). $c_{\max} = 0.177\ \mu\mathrm{m}^{-1}$ for $L = T/c_{\max}$. Input wavelength $\lambda = 1550$ nm.

the fastest possible state evolution achievable under a given tolerable crosstalk $\bar{p}_{\pm1}^{\max}$—has thus been demonstrated.

To experimentally validate the feasibility of inverse design, we implement the four aforementioned cases on a silicon-on-insulator (SOI) photonic waveguide platform, as illustrated in Fig. 3(c) [18,41,42]. Details regarding the waveguide parameters, sample fabrication, and experimental measurement setup are provided in Ref. [37]. Figures 3(e)–3(h) present full-wave simulations performed using COMSOL Multiphysics. The simulation results are in good agreement with the analysis in Fig. 3(b), where the intensity observed in the intermediate waveguide serves as an indicator of the system's adiabatic behavior. In experiments, the waveguide arrays, input grating couplers, and extended output ports were fabricated using electron-beam lithography (EBL, Eliomix ELS-F125) and dry etching (Oxford PP100). We coupled the laser light into the waveguide lattice via an input grating coupler. The transmitted light scattered from the extended output ports was collected, and the coupling-in and coupling-out processes were imaged using a near-infrared charge-coupled device (CCD) camera in Fig. 3(d). For the four STIRAP lattices in Figs. 3(i)–3(l), the output optical fields were measured at $z = 0.25L$, $0.5L$, $0.75L$, and $L$, respectively. The experimental results agree well with simulations, confirming the feasibility of the inverse design strategy in photonic waveguides.

The optimal STIRAP evolution has been achieved using inverse adiabaticity control, with its feasibility experimentally demonstrated. We now turn to a more detailed discussion of the results from this new landscape. Figure 4(a) compares several typical conventional designs, including linear, Gaussian–exponential, CD protocol, and IIE schemes. Given a coupling profile $X$ and $T$, $F_0$, and $\bar{p}_{\pm1}$ can be evaluated. A design is considered valid if $F_0 > 0.99$, and its location in the $(\bar{p}_{\pm1}^{\max}, T)$ space can then be identified. Although several valid points appear, none lie exactly on the ACL [marked points in Fig. 4(a)], implying structural redundancy. In contrast, inverse design has the ability to yield solutions precisely on the ACL, ensuring maximum compactness (see Ref. [37] for detailed comparisons).

Importantly, solutions on the ACL also demonstrate superior robustness. To verify this, we introduce random diagonal detuning disorders of strength $\Delta$: $\tilde{\Delta}_n = c_{\max}\Delta\delta$, $n = 1, 2, 3$, which are known to cause significant performance degradation in integrated photonic devices. Figure 4(a) illustrates the standard deviation of fidelity $\sigma_0$ for inverse-designed structures subjected to a substantial disorder strength of $\Delta = 0.3$. It is evident that proximity to the ACL results in decreased variability in fidelity. Figure 4(b) shows the average fidelity $\bar{F}_0$ and its variation $\sigma_0$ over different $T$ at $\bar{p}_{\pm1}^{\max} = 0.45$. Notably, at the ACL point where $T = 2.4$, the system achieves maximum fidelity accompanied by relatively low variability. Conversely, unnecessarily prolonged evolution times result in decreased fidelity and increased variability, signifying a drop in performance.

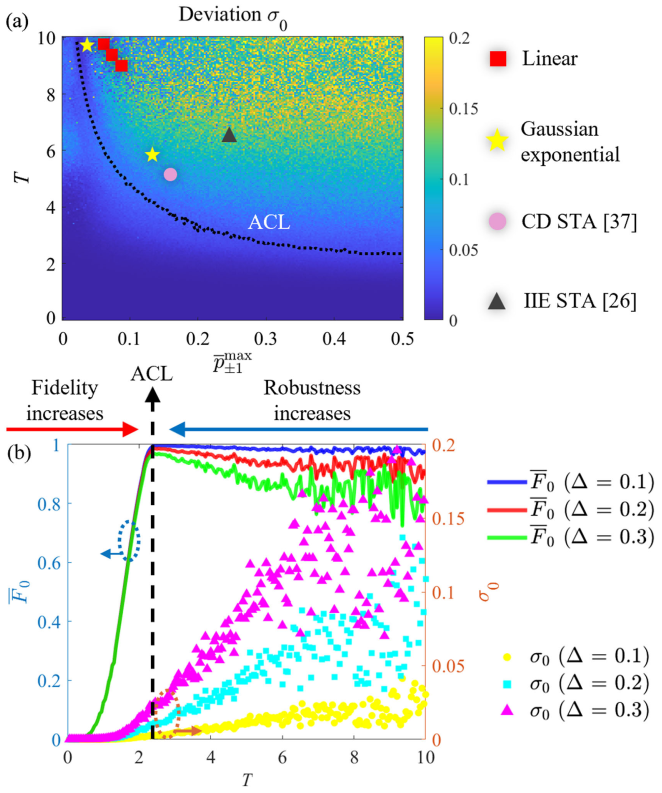

FIG. 4. (a) The standard deviations of fidelity $\sigma_0$ with respect to evolving time $T$ and tolerable crosstalk $\bar{p}_{\pm1}^{\max}$ under a structural deviation degree of $\Delta = 0.3$. The dotted line indicates the ACL. The marked points correspond to the results $(\bar{p}_{\pm1}, T)$ of forward designed structures satisfying $F_0 > 0.99$. (b) The mean values of fidelity $\bar{F}_0$ and the standard deviations of fidelity $\sigma_0$ with respect to varying $T$ and $\Delta$ at fixed $\bar{p}_{\pm1}^{\max} = 0.45$. The dotted line indicates the ACL point (0.45, 2.4). Each data point is derived from 100 independent simulation runs. Detailed parameters and more results of robustness are provided in Ref. [37].

Once the target outcome is ensured, the reduced redundancy actually enhances robustness. The ACL precisely defines the optimal frontier where such redundancy is eliminated. It achieves the shortest possible evolution time under the same tolerable crosstalk, corresponding to optimal compactness, and simultaneously yields the smallest average crosstalk among all solutions with the same duration, ensuring the highest robustness against perturbations. In contrast, solutions not lying on the ACL inevitably undergo unnecessary additional crosstalk, which increase the likelihood of deviation from the target state [37]. In this sense, the degradation of robustness in conventional STA designs does not merely stem from the simple introduction of crosstalk, but from the fact that these designs fail to follow the ACL, thereby introducing redundant average crosstalk. This finding highlights the critical role of the ACL, where compactness and robustness—two essential attributes for large-scale photonic integration and high-precision quantum computation—are simultaneously optimized.

In conclusion, we have constructed a comprehensive and optimal landscape of (non-) adiabatic state evolution by introducing an optimization-based inverse design framework. Using STIRAP as a representative case, we demonstrated how inverse design systematically identifies optimal strategies that achieve the target output with high fidelity. As a proof of principle, we experimentally validated these designs in integrated silicon waveguides, confirming optimal compactness compared to conventional forward-designed structures. Crucially, our approach enables access to the ACL, thereby eliminating redundant evolution and achieving optimal robustness performance—a key requirement for practical quantum and photonic applications. Beyond the specific case studied here, the method can be readily extended to more complex systems [37]. Our results provide broadly applicable tool for precise and flexible control of (non-) adiabatic state evolution, providing new opportunities for a wide range of quantum and integrated photonic devices, such as adiabatic quantum computation [12,43], non-Abelian quantum logic gate [13,42,44–46] and quantum sensor [14,47].

*Acknowledgments*—The authors acknowledge the financial support from National Natural Science Foundation of China (No. 62288101, No. 62325504, No. 12522421, No. 12204233, and No. 12174186). T. L. thanks the support from Dengfeng Project B of Nanjing University.

The authors declare no conflicts of interest.

*Data availability*—The data that support the findings of this article are not publicly available. The data are available from the authors upon reasonable request.

[1] S. Pancharatnam, Generalized theory of interference, and its applications, Proc. Indian Acad. Sci. **44**, 247 (1956).
[2] M. V. Berry, Quantal phase factors accompanying adiabatic changes, Proc. R. Soc. A **392**, 45 (1984).
[3] J. H. Hannay, Angle variable holonomy in adiabatic excursion of an integrable Hamiltonian, J. Phys. A **18**, 221 (1985).
[4] J. R. Kuklinski, U. Gaubatz, F. T. Hioe, and K. Bergmann, Adiabatic population transfer in a three-level system driven by delayed laser pulses, Phys. Rev. A **40**, 6741 (1989).
[5] U. Gaubatz, P. Rudecki, S. Schiemann, and K. Bergmann, Population transfer between molecular vibrational levels by stimulated Raman scattering with partially overlapping laser fields. A new concept and experimental results, J. Chem. Phys. **92**, 5363 (1990).
[6] T. A. Laine and S. Stenholm, Adiabatic processes in three-level systems, Phys. Rev. A **53**, 2501 (1996).
[7] K. Bergmann, H. Theuer, and B. W. Shore, Coherent population transfer among quantum states of atoms and molecules, Rev. Mod. Phys. **70**, 1003 (1998).

[8] K. Bergmann, N. V. Vitanov, and B. W. Shore, Perspective: Stimulated Raman adiabatic passage: The status after 25 years, J. Chem. Phys. **142**, 170901 (2015).

[9] N. V. Vitanov, A. A. Rangelov, B. W. Shore, and K. Bergmann, Stimulated Raman adiabatic passage in physics, chemistry, and beyond, Rev. Mod. Phys. **89**, 015006 (2017).

[10] D. J. Thouless, Quantization of particle transport, Phys. Rev. B **27**, 6083 (1983).

[11] R. Citro and M. Aidelsburger, Thouless pumping and topology, Nat. Rev. Phys. **5**, 87 (2023).

[12] T. Albash and D. A. Lidar, Adiabatic quantum computation, Rev. Mod. Phys. **90**, 015002 (2018).

[13] Y. Yang, B. Yang, G. Ma, J. Li, S. Zhang, and C. T. Chan, Non-Abelian physics in light and sound, Science **383**, eadf9621 (2024).

[14] C. L. Degen, F. Reinhard, and P. Cappellaro, Quantum sensing, Rev. Mod. Phys. **89**, 035002 (2017).

[15] W. Bogaerts and L. Chrostowski, Silicon photonics circuit design: Methods, tools and challenges, Laser Photonics Rev. **12**, 1700237 (2018).

[16] P. Cheben, R. Halir, J. H. Schmid, H. A. Atwater, and D. R. Smith, Subwavelength integrated photonics, Nature (London) **560**, 565 (2018).

[17] S. Shekhar, W. Bogaerts, L. Chrostowski, J. E. Bowers, M. Hochberg, R. Soref, and B. J. Shastri, Roadmapping the next generation of silicon photonics, Nat. Commun. **15**, 751 (2024).

[18] S. Wu, W. Song, J. Sun, J. Li, Z. Lin, X. Liu, S. Zhu, and T. Li, Approaching the adiabatic infimum of topological pumps on thin-film lithium niobate waveguides, Nat. Commun. **15**, 9805 (2024).

[19] A. A. Stepanenko, K. S. Chernova, and M. A. Gorlach, Time-optimal transfer of the quantum state in long qubit arrays, Phys. Rev. Lett. **135**, 010803 (2025).

[20] D. Guéry-Odelin, A. Ruschhaupt, A. Kiely, E. Torrontegui, S. Martínez-Garaot, and J. G. Muga, Shortcuts to adiabaticity: Concepts, methods, and applications, Rev. Mod. Phys. **91**, 045001 (2019).

[21] T. Hatomura, Shortcuts to adiabaticity: Theoretical framework, relations between different methods, and versatile approximations, J. Phys. B **57**, 102001 (2024).

[22] M. Demirplak and S. A. Rice, On the consistency, extremal, and global properties of counterdiabatic fields, J. Chem. Phys. **129**, 154111 (2008).

[23] M. V. Berry, Transitionless quantum driving, J. Phys. A **42**, 365303 (2009).

[24] X. Chen, I. Lizuain, A. Ruschhaupt, D. Guéry-Odelin, and J. G. Muga, Shortcut to adiabatic passage in two- and three-level atoms, Phys. Rev. Lett. **105**, 123003 (2010).

[25] X. Chen, E. Torrontegui, and J. G. Muga, Lewis-Riesenfeld invariants and transitionless quantum driving, Phys. Rev. A **83**, 062116 (2011).

[26] X. Chen and J. G. Muga, Engineering of fast population transfer in three-level systems, Phys. Rev. A **86**, 033405 (2012).

[27] S. K. Turitsyn, A. E. Bednyakova, M. P. Fedoruk, S. B. Papernyi, and W. R. L. Clements, Inverse four-wave mixing and self-parametric amplification in optical fibre, Nat. Photonics **9**, 608 (2015).

[28] S. Molesky, Z. Lin, A. Y. Piggott, W. Jin, J. Vucković, and A. W. Rodriguez, Inverse design in nanophotonics, Nat. Photonics **12**, 659 (2018).

[29] L. Ma, J. Li, Z. Liu, Y. Zhang, N. Zhang, S. Zheng, and C. Lu, Intelligent algorithms: New avenues for designing nanophotonic devices [Invited], Chin. Optic. Lett. **19**, 011301 (2021).

[30] Z. Li, R. Pestourie, J.-S. Park, Y.-W. Huang, S. G. Johnson, and F. Capasso, Inverse design enables large-scale high-performance meta-optics reshaping virtual reality, Nat. Commun. **13**, 2409 (2022).

[31] Diogo E. P. Pinto, Nuno A. M. Araújo, P. Šulc, and J. Russo, Inverse design of self-folding 3D shells, Phys. Rev. Lett. **132**, 118201 (2024).

[32] S. Xia *et al.*, Deep-learning-empowered synthetic dimension dynamics: Morphing of light into topological modes, Adv. Opt. Photonics **6**, 026005 (2024).

[33] J. Liao, Y. Tian, Z. Yang, H. Xu, C. Tang, Y. Wang, X. Zhang, and Z. Kang, Inverse design of highly efficient and broadband mode splitter on SOI platform, Chin. Optic. Lett. **22**, 011302 (2024).

[34] H. Li, J. Deng, J. Feng, L. Zhao, Z. Shen, G. Xia, Z. Wu, J. Wu, and J. Yang, Single-point tunable and non-volatile Y-junction photonic power splitter on SOI with broadband and low loss, Chin. Optic. Lett. **23**, 022201 (2025).

[35] Average crosstalk refers to the time-averaged sum of the population (occupation probability) of all other nontarget modes over the evolution process. The precise mathematical expression for this definition is provided in the description of Fig. 2(c).

[36] A. Yariv, Coupled-mode theory for guided-wave optics, IEEE J. Quantum Electron. **9**, 919 (1973).

[37] See Supplemental Material at http://link.aps.org/supplemental/10.1103/zwt9-79zy for discussion about details of the optimization settings, coupling coefficient profiles of inverse-designed results, more results of zero-mode population, advantages of the inverse design over conventional forward design, experimental measurements, fabrication of the silicon waveguides, robustness of inverse-designed results, and inverse design of SSH topological pumping, which includes Refs. [18,19,21–26,38–40].

[38] M. Born and V. Fock, Beweis des adiabatensatzes, Z Med. Phys. **51**, 165 (1928).

[39] W. Liu, C. Wu, Y. Jia, S. Jia, G. Chen, and F. Chen, Observation of edge-to-edge topological transport in a photonic lattice, Phys. Rev. A **105**, L061502 (2022).

[40] C. Wu, W. Liu, Y. Jia, G. Chen, and F. Chen, Observation of topological pumping of a defect state in a Fock photonic lattice, Phys. Rev. A **107**, 033501 (2023).

[41] S. Wu, W. Song, J. Sun, Z. Lin, H. Xin, S. Zhu, and T. Li, Broadband asymmetric light transport in compact lithium niobate waveguides, Laser Photonics Rev. **17**, 2300306 (2023).

[42] X.-L. Zhang, F. Yu, Z.-G. Chen, Z.-N. Tian, Q.-D. Chen, H.-B. Sun, and G. Ma, Non-Abelian braiding on photonic chips, Nat. Photonics **16**, 390 (2022).

[43] E. K. Grant and T. S. Humble, *Adiabatic Quantum Computing and Quantum Annealing*. Oxford Research Encyclopedia of Physics (Oxford University Press, New York, 2020), 10.1093/acrefore/9780190871994.013.32.

[44] Z.-G. Chen, R.-Y. Zhang, C. T. Chan, and G. Ma, Classical non-Abelian braiding of acoustic modes, Nat. Phys. **18**, 179 (2022).

[45] Z. X. Chen, L. L. Ma, S. J. Ge, Z.-G. Chen, M. H. Lu, Y. F. Chen, and Y. Q. Lu, Transient logic operations in acoustics through dynamic modulation, Phys. Rev. Appl. **21**, L011001 (2024).

[46] W. Song, X. Liu, J. Sun, O. You, S. Wu, C. Chen, S. Zhu, T. Li, and S. Zhang, Shortcuts to adiabatic non-Abelian braiding on silicon photonic chips, Sci. Adv. **11**, eadt7224 (2025).

[47] S. D. Bass and M. Doser, Quantum sensing for particle physics, Nat. Rev. Phys. **6**, 329 (2024).